Supplementary Information (SI) for Digital Discovery.
This journal is © The Royal Society of Chemistry 2026

Electronic Supplementary Information

Data-driven exploration of AB_2X_4 (X=O, S, Se, Te) spinel chemical space

Panyalak Detrattanawichai,[a] Zhenzhu Li,[a] Hyunsoo Park,[a] Kinga O. Mastej,[a] and Aron Walsh[a]*

[a]Department of Materials, Imperial College London, London SW7 2AZ, UK

E-mail: a.walsh@imperial.ac.uk

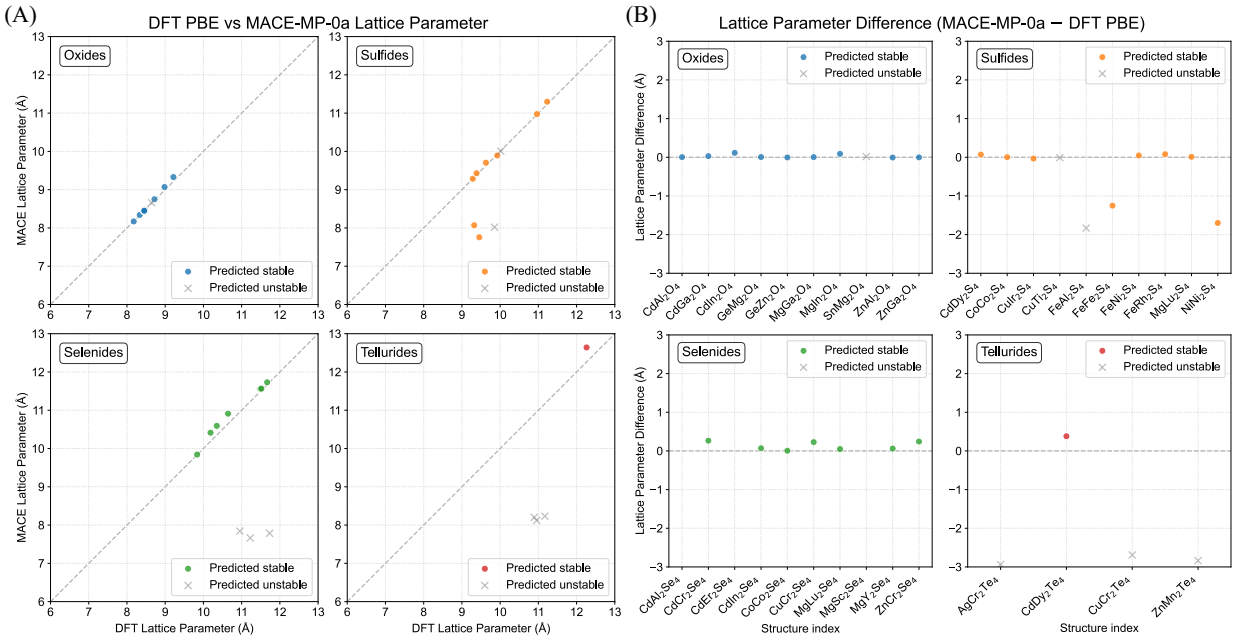

Fig. S1 (A) Parity and (B) difference plots of DFT and MACE-MP-0a calculated lattice parameters of experimentally known oxide and chalcogenide spinels. Predicted stable compositions are shown in colored while predicted unstable ones are shown in grey crossed symbol.

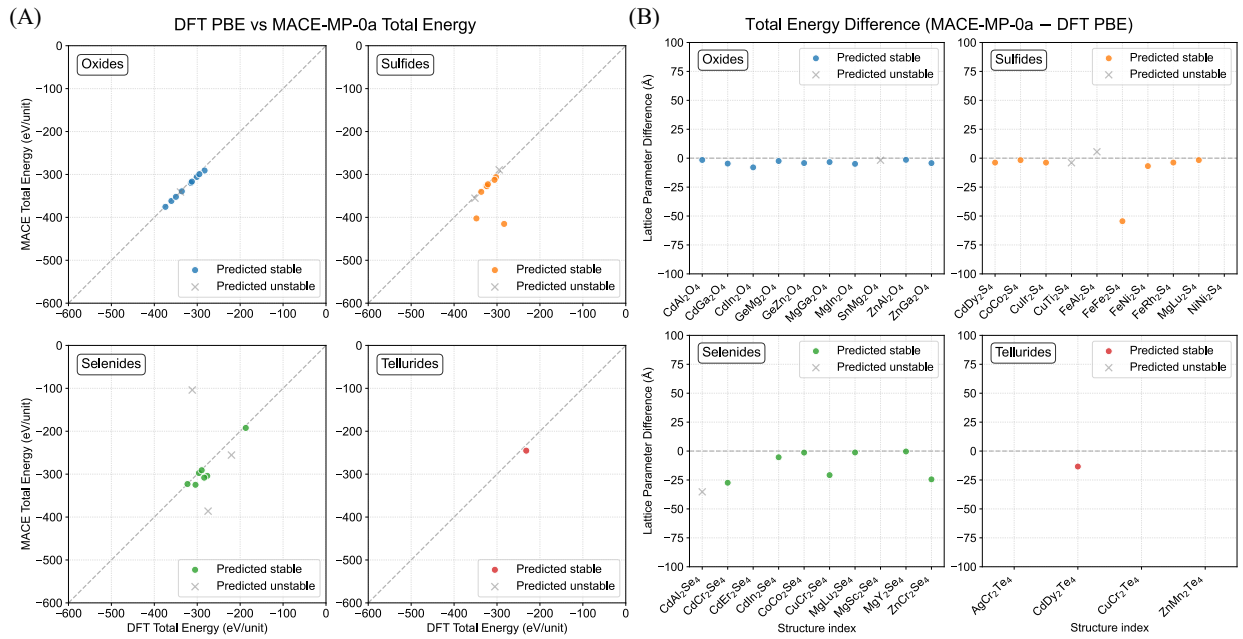

Fig. S2 (A) Parity and (B) difference plots of DFT and MACE-MP-0a calculated total energies per unit of experimentally known oxide and chalcogenide spinels.

To compare results from MACE-MP-0a against Density Functional Theory (DFT),[1,2] first-principles calculations using DFT framework were employed with Generalized Gradient Approximation (GGA) by Perdew-Berke-Ernzerhof (PBE)[3]. The Projector Augmented Wave (PAW)[4,5] pseudopotentials as defined within Vienna Ab initio Simulation Package (VASP)[6,7] were used to describe the interactions between ion cores and valence electrons. An energy cutoff of 520 eV was selected to optimise the structures until the force on each atom is less than 0.01 eV/Å and the energy convergence reaches 10^{-6} eV with Gamma 4×4×4 *k*-point for all systems alongside Gaussian smearing with a width of 0.05 eV. For MACE[8–10] calculations, the settings are mentioned in the main manuscript. The results are shown in Fig. S1 and Fig. S2.

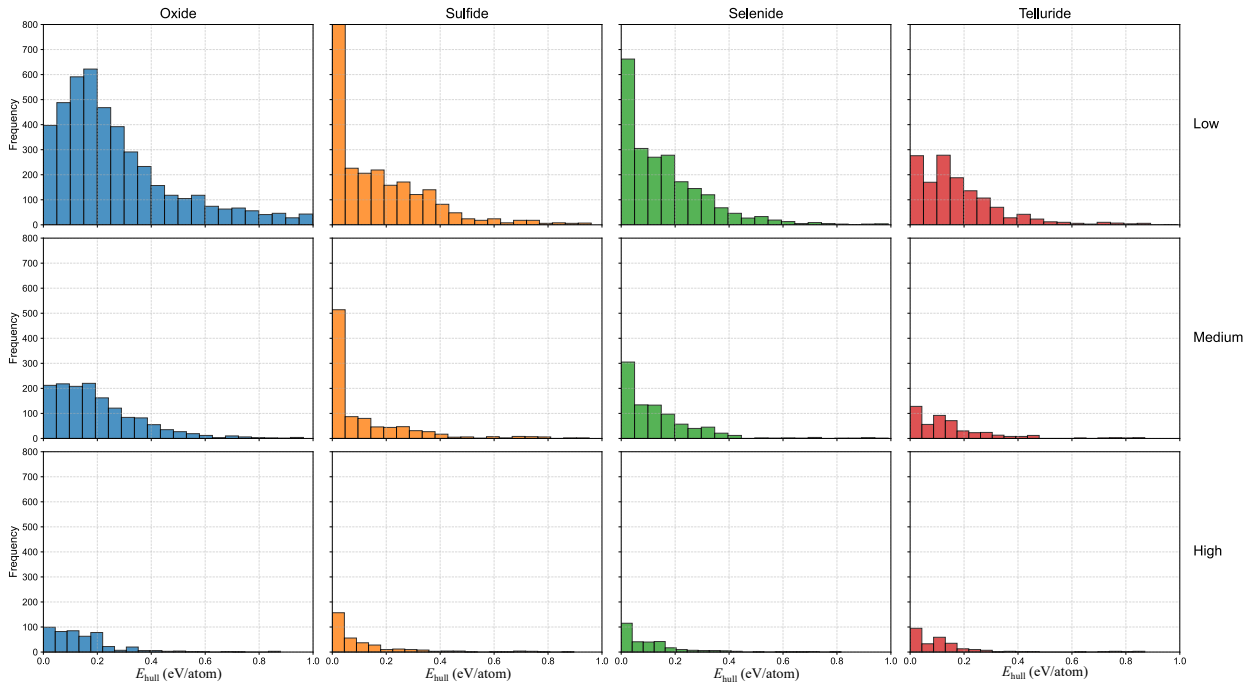

Fig. S3 E_{hull} distribution for four types of anions with different oxidation state thresholds

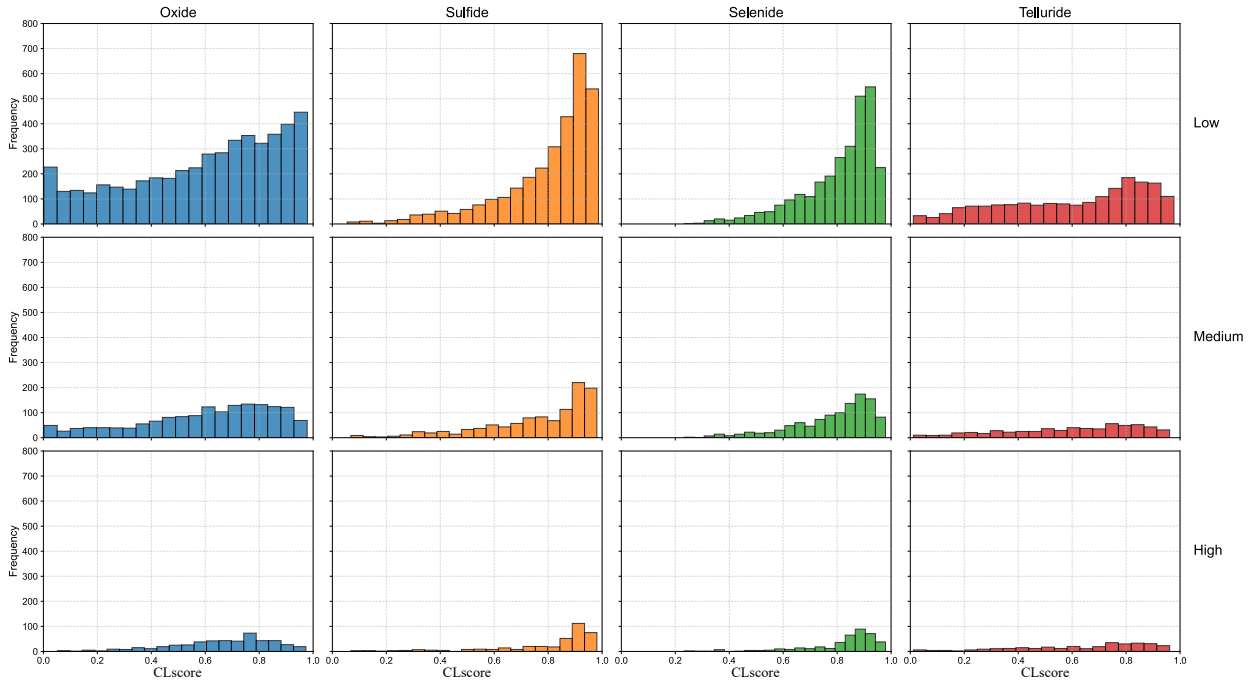

Fig. S4 CLscore distribution for four types of anions with different oxidation state thresholds

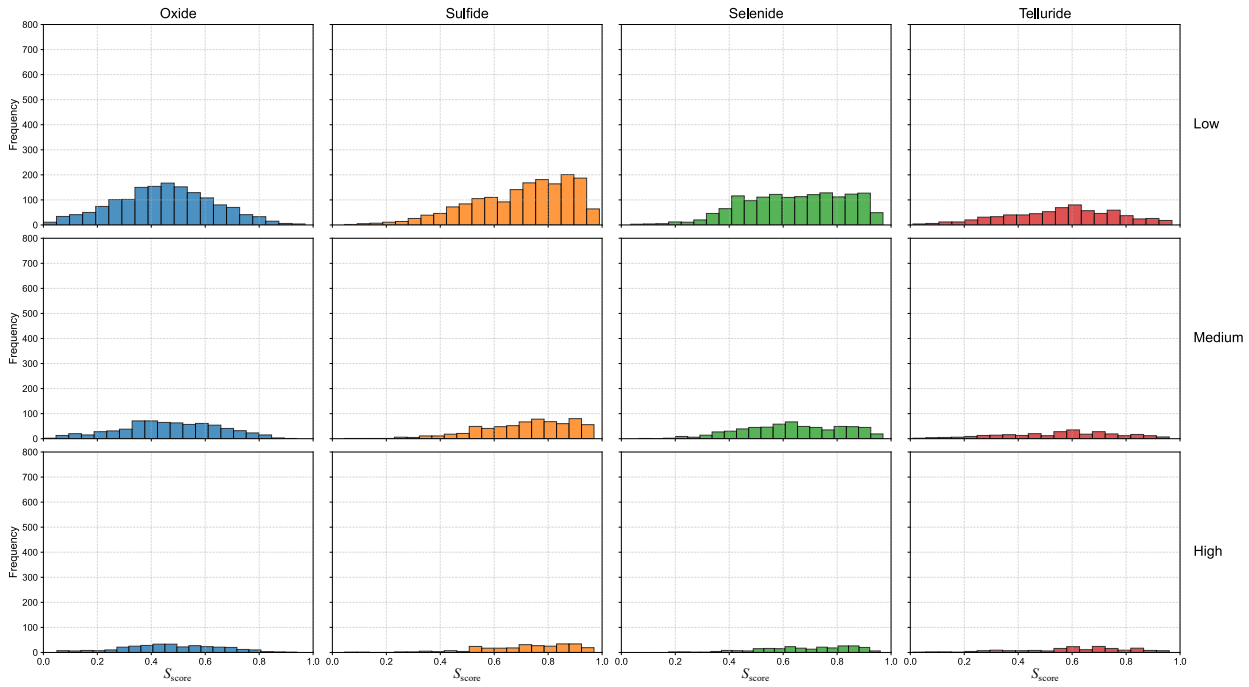

Fig. S5 S_{score} distribution for four types of anions with different oxidation state thresholds

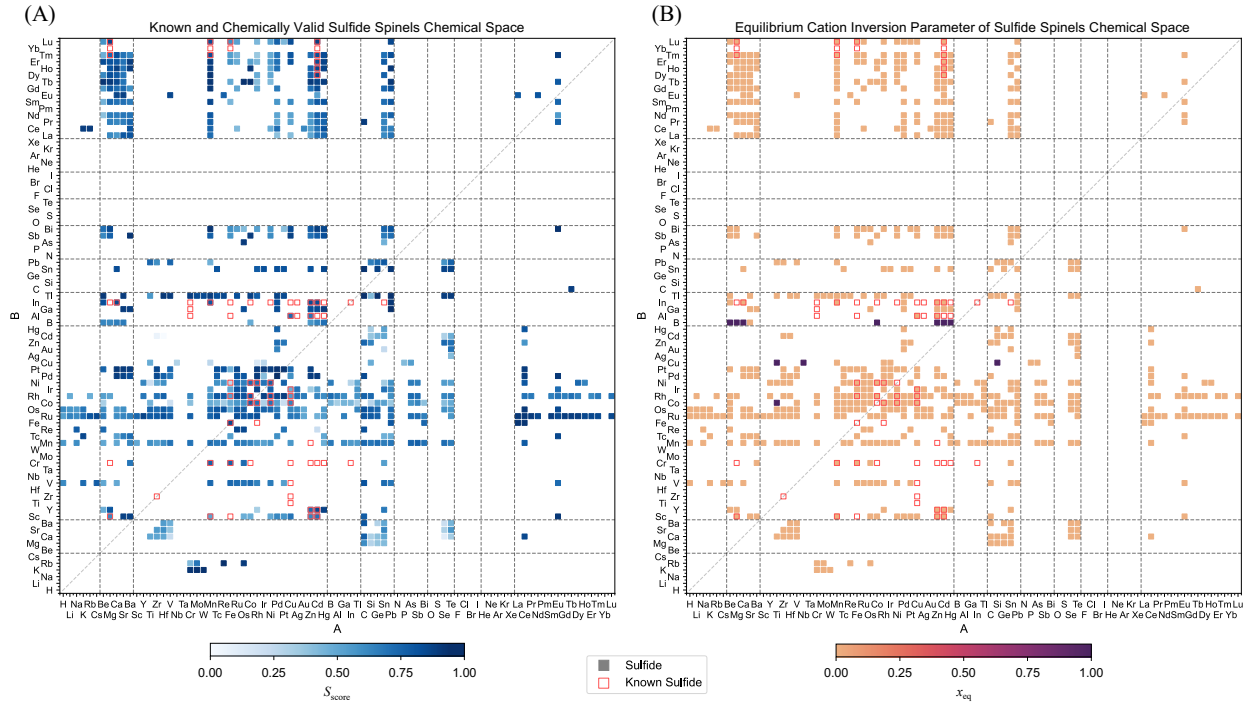

Fig. S6 Chemical space of sulfide spinels that satisfy both $E_{hull} \leq 0.2$ eV/atom AND CLscore ≥ 0.5. (A) The blue gradient indicates S_{score}, where lighter and darker shades designate lower and higher crystal likelihood, respectively. (B) The colourmap represents the equilibrium cation inversion

parameter x_{eq}, where lighter orange designates the normal configuration, and darker purple represents the inverse configuration. The red square markers denote the experimentally known spinel compositions.

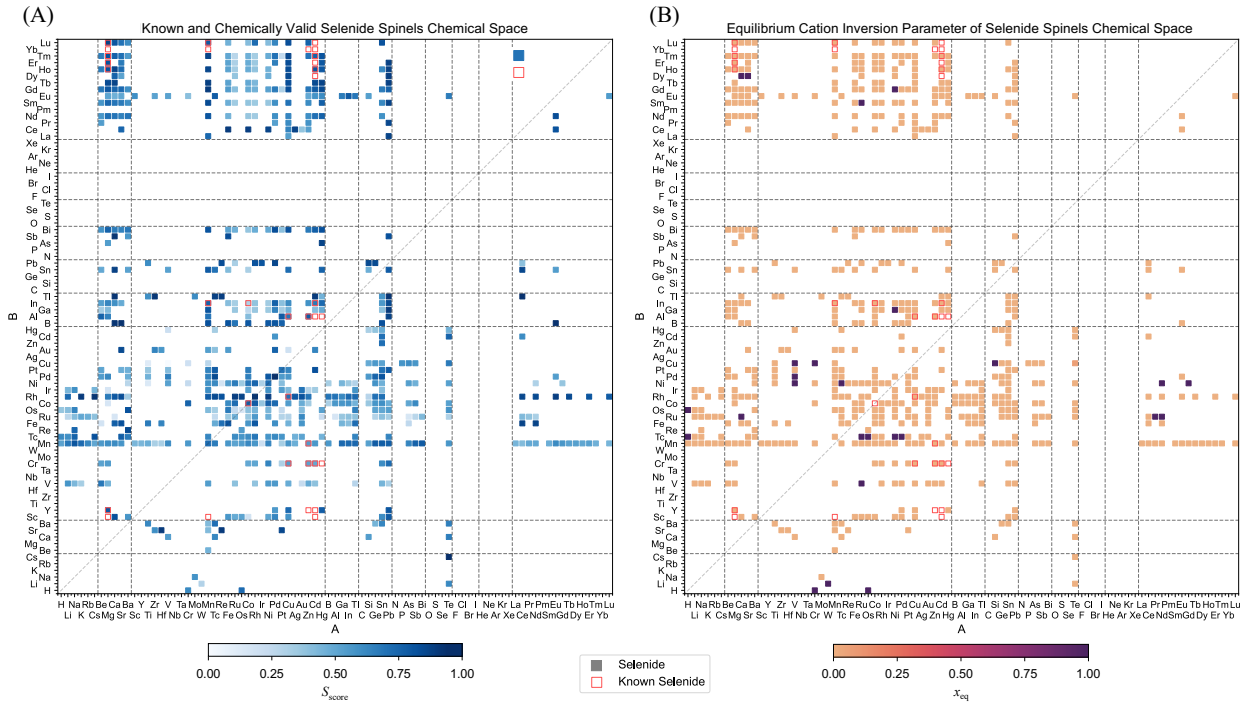

Fig. S7 Chemical space of selenide spinels that satisfy both $E_{hull} \leq 0.2$ eV/atom AND CLscore $\geq$ 0.5. (A) The blue gradient indicates S_{score}, where lighter and darker shades designate lower and higher crystal likelihood, respectively. (B) The colourmap represents the equilibrium cation inversion parameter x_{eq}, where lighter orange designates the normal configuration, and darker purple represents the inverse configuration. The red square markers denote the experimentally known spinel compositions.

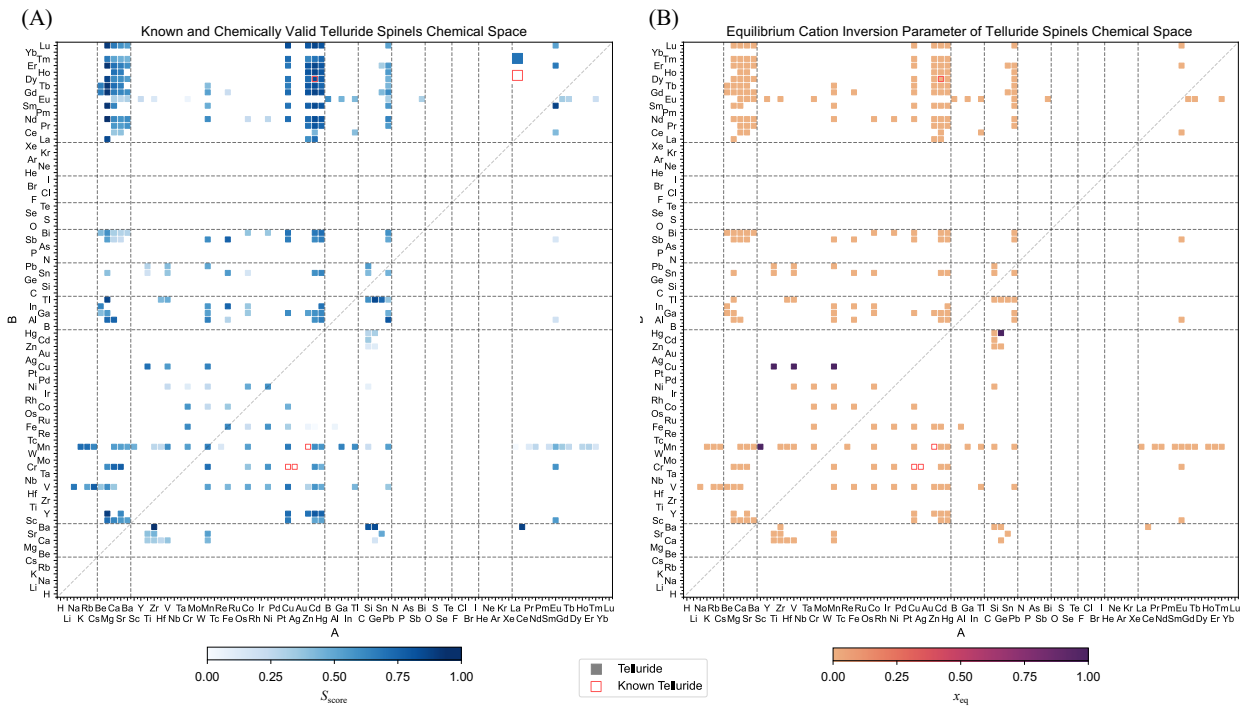

Fig. S8 Chemical space of telluride spinels that satisfy both $E_{hull} \leq 0.2$ eV/atom AND CLscore $\geq$ 0.5. (A) The blue gradient indicates S_{score}, where lighter and darker shades designate lower and higher crystal likelihood, respectively. (B) The colourmap represents the equilibrium cation inversion parameter x_{eq}, where lighter orange designates the normal configuration, and darker purple represents the inverse configuration. The red square markers denote the experimentally known spinel compositions.

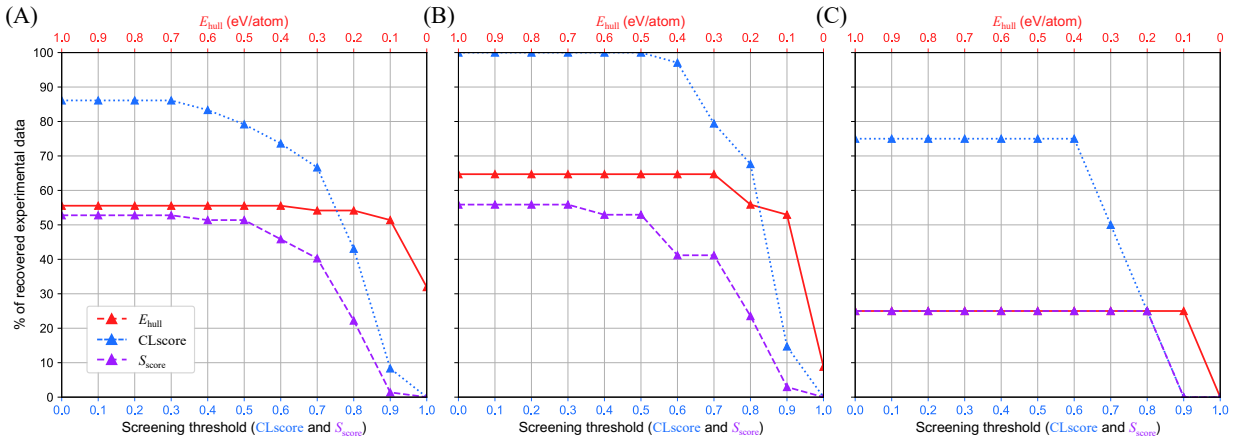

Fig. S9 Fraction of recovered experimentally known (A) sulfide, (B) selenide, and (C) telluride spinels with medium oxidation state threshold for the initial chemical filter.

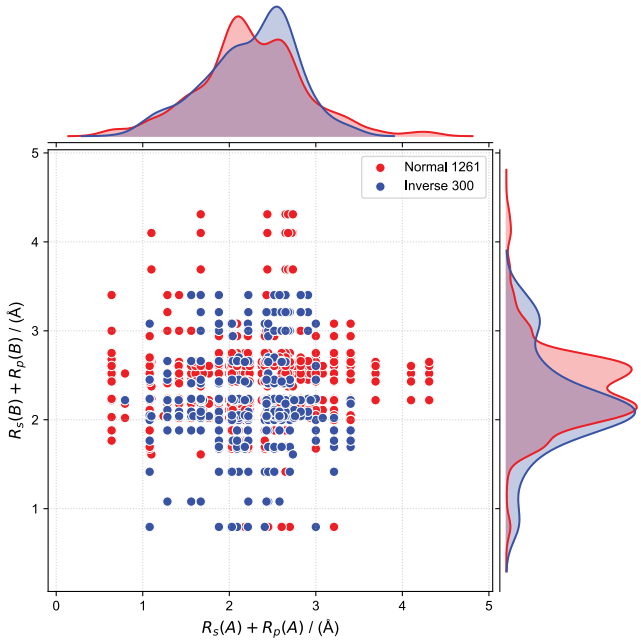

Fig. S10 Orbital-radii separation map of AB_2X_4 spinels (X=O, S, Se, Te) with preferred normal and inverse configurations, determined by E_{hull}, in red and blue, respectively.

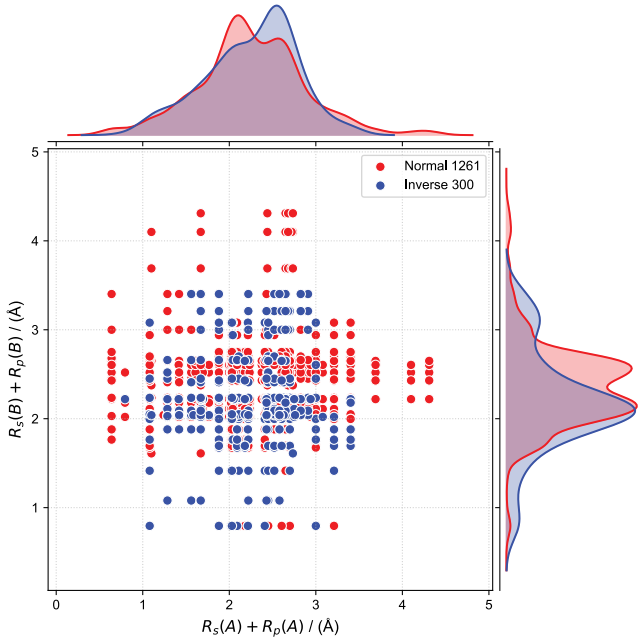

Fig. S11 Orbital-radii separation map of AB_2X_4 spinels (X=O, S, Se, Te) with preferred normal and inverse configurations, determined by x_{eq}, in red and blue, respectively.

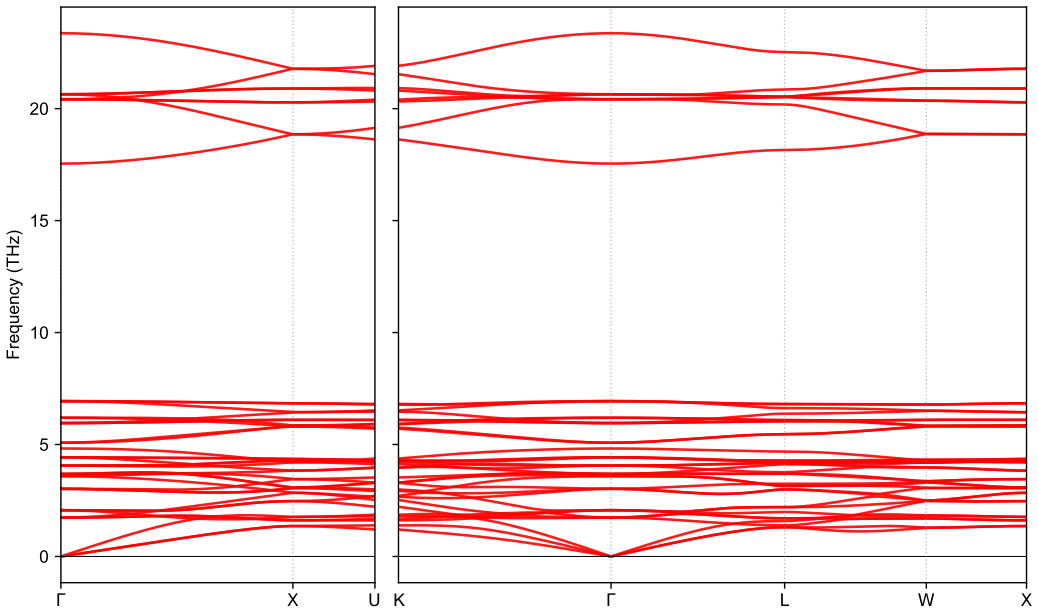

Fig. S12 Phonon band structure of ReK_2O_4

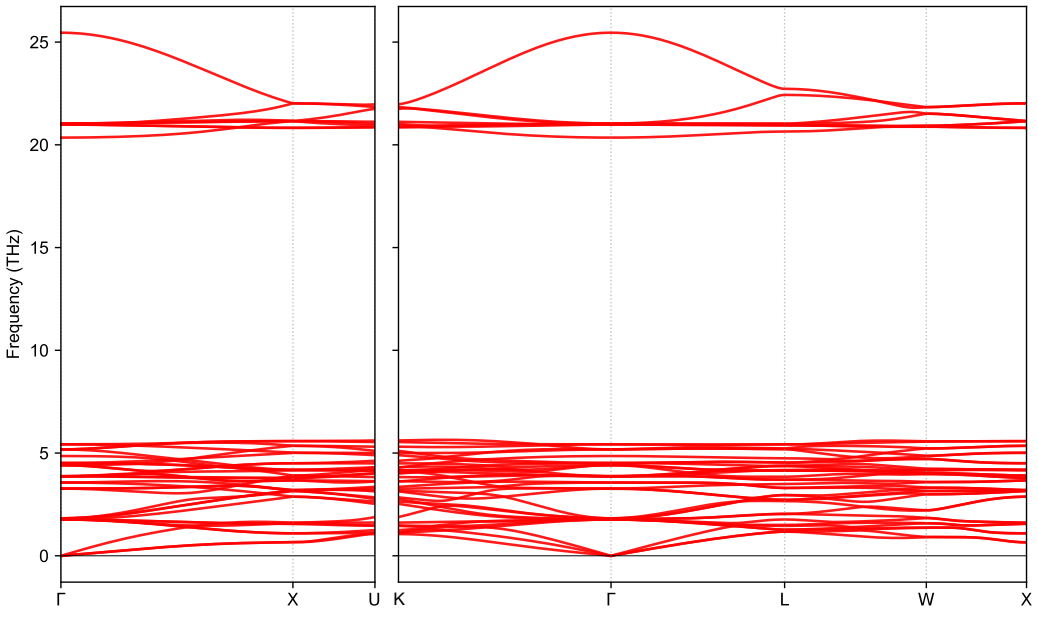

Fig. S13 Phonon band structure of OsK_2O_4

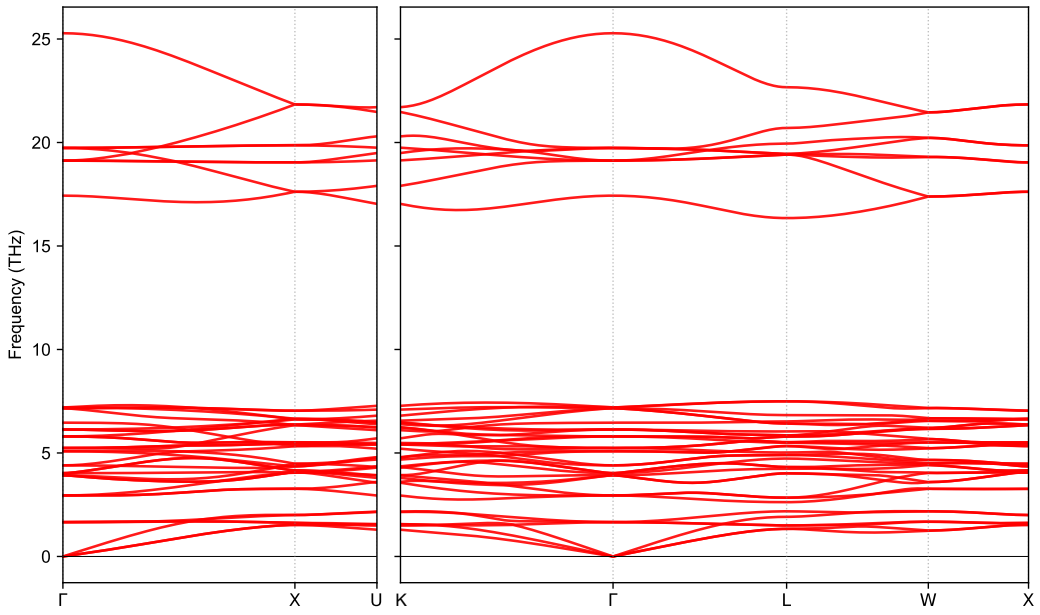

Fig. S14 Phonon band structure of $ReNa_2O_4$

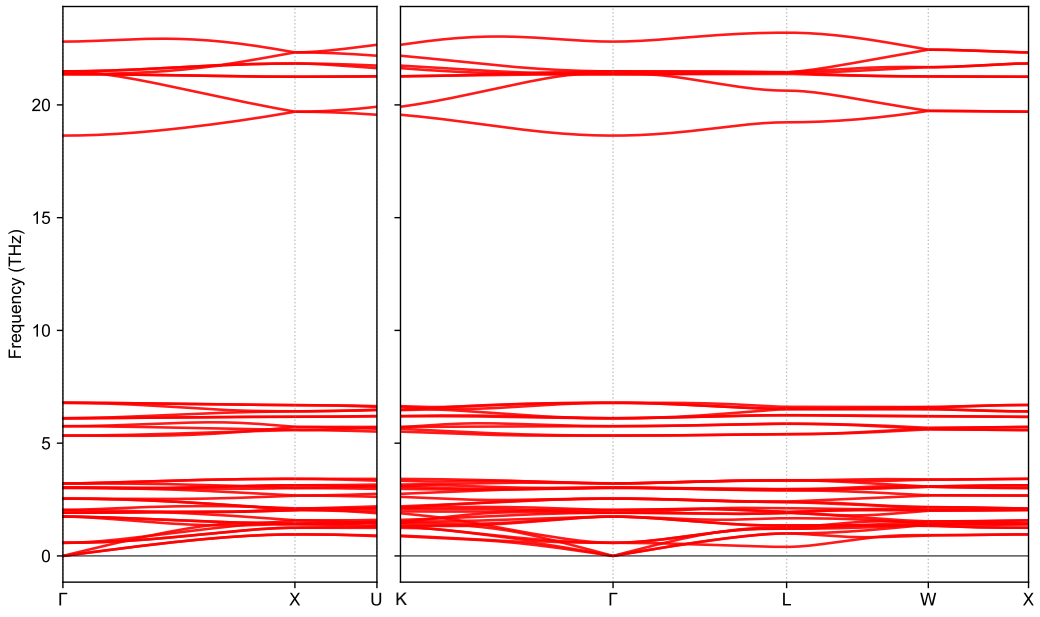

Fig. S15 Phonon band structure of $ReRb_2O_4$

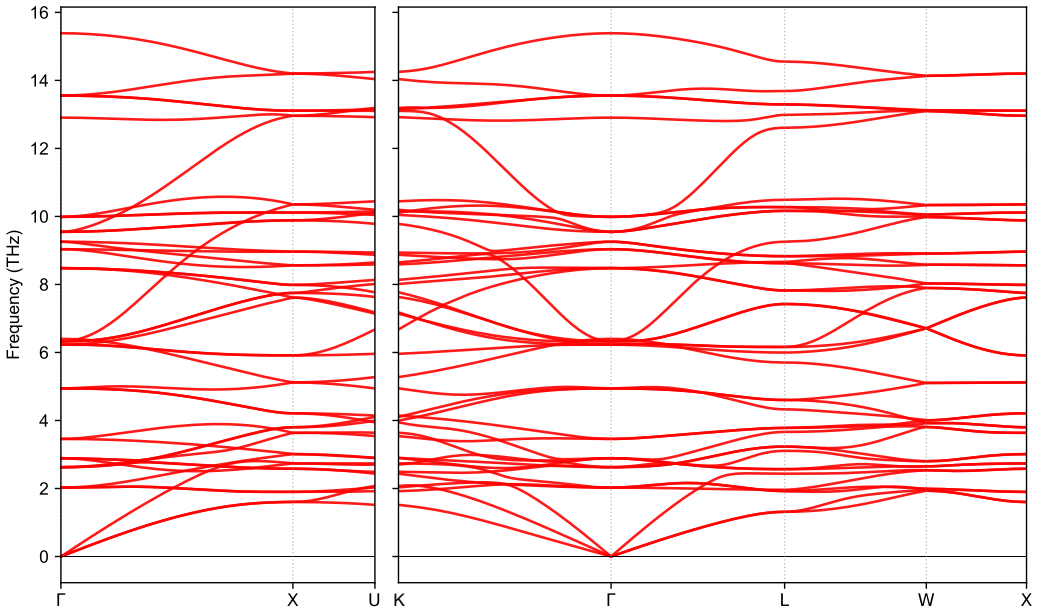

Fig. S16 Phonon band structure of $BaNd_2O_4$

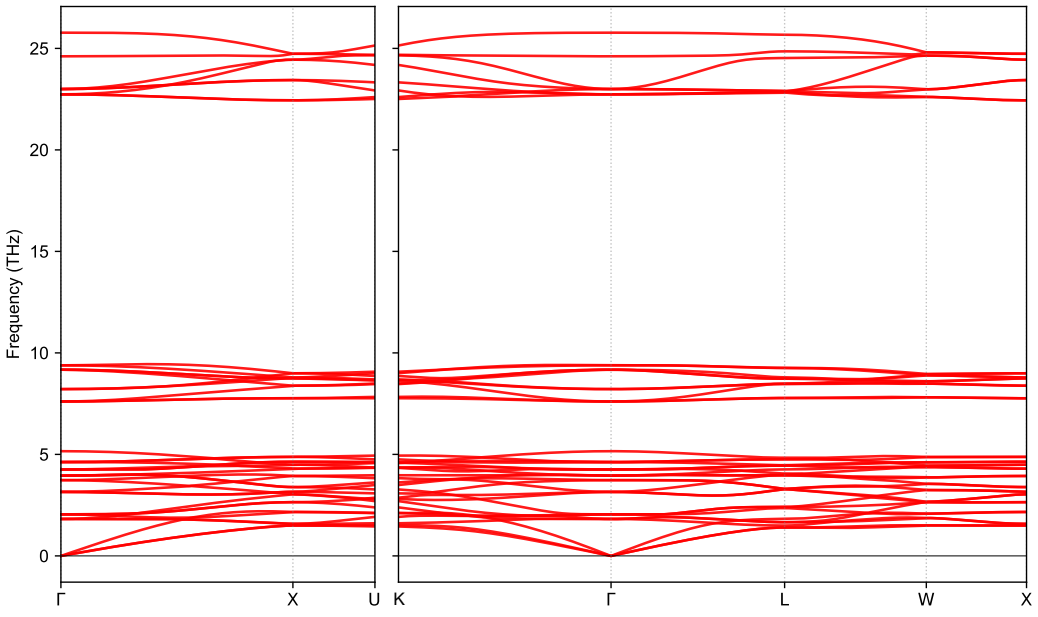

Fig. S17 Phonon band structure of WK_2O_4

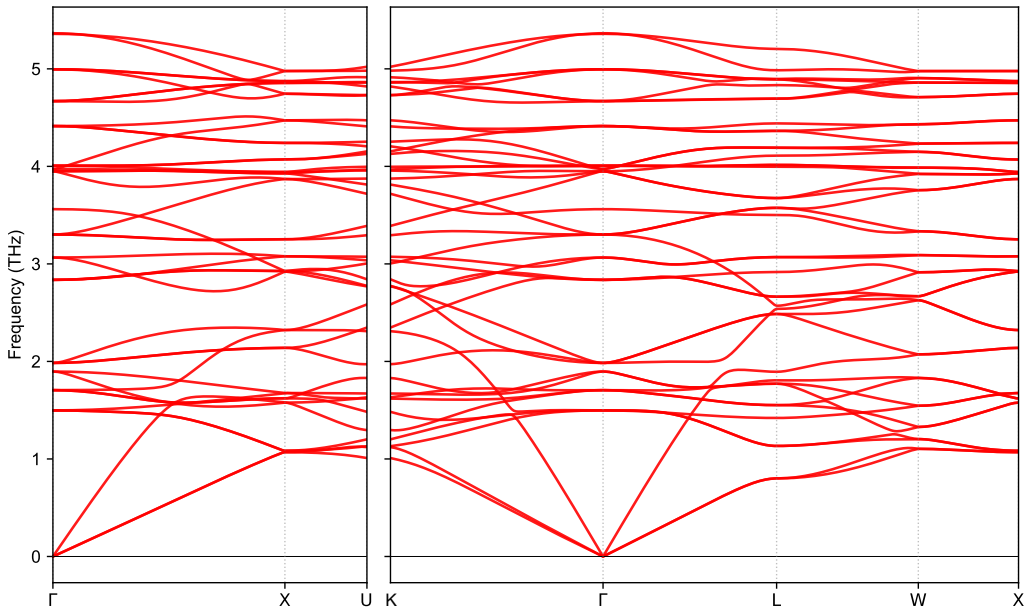

Fig. S18 Phonon band structure of Pd_3Se_4

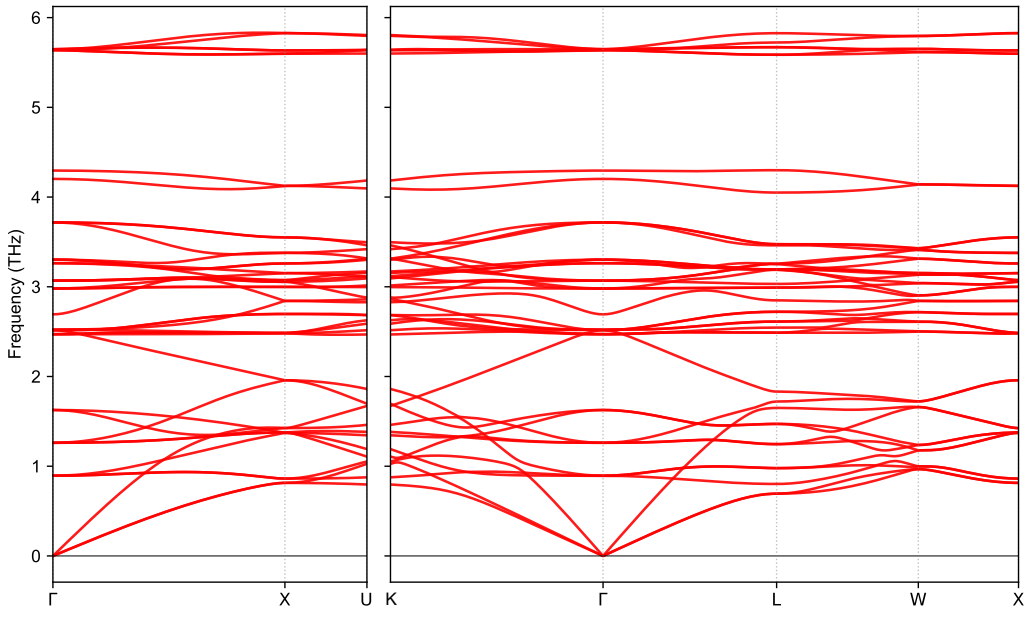

Fig. S19 Phonon band structure of $MgNd_2Te_4$

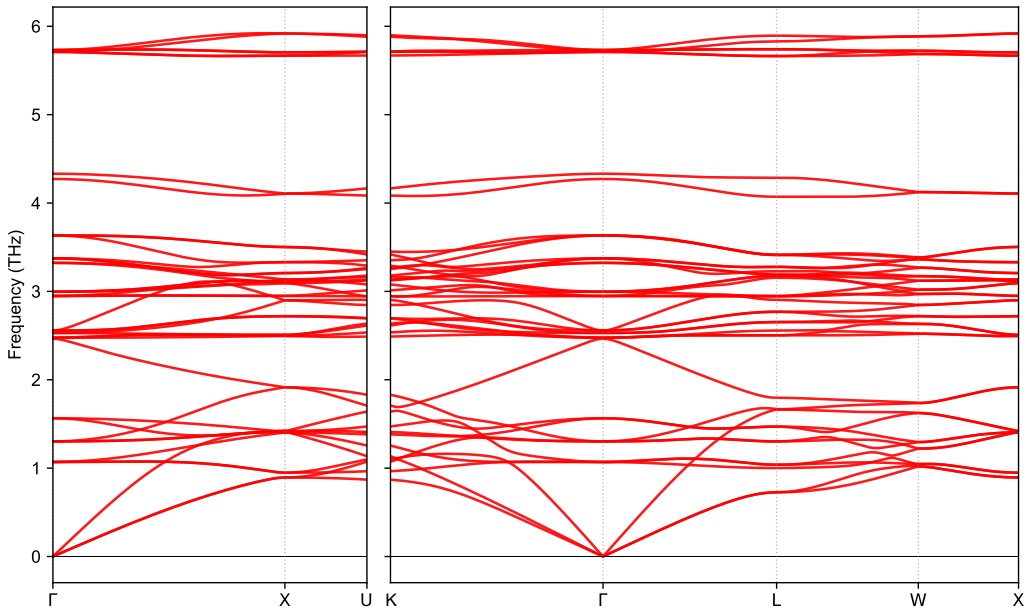

Fig. S20 Phonon band structure of $MgEr_2Te_4$

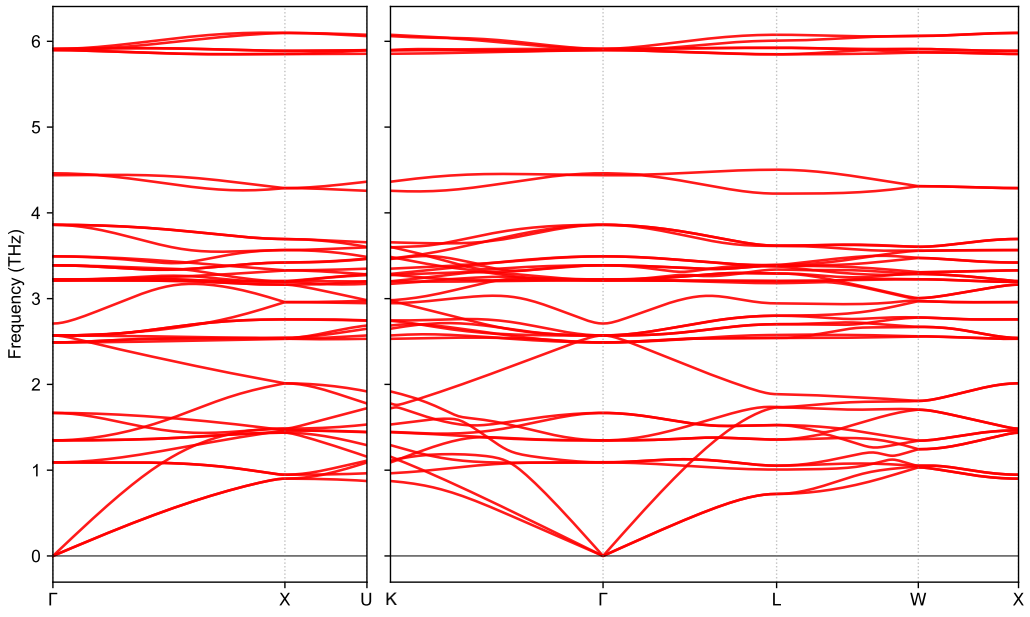

Fig. S21 Phonon band structure of $MgTb_2Te_4$

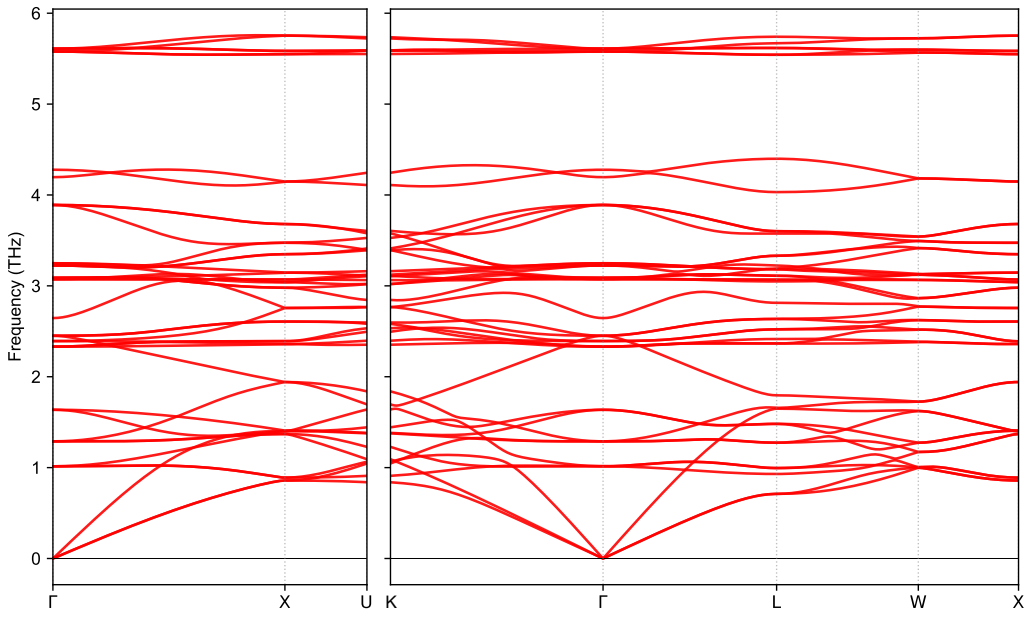

Fig. S22 Phonon band structure of $MgGd_2Te_4$

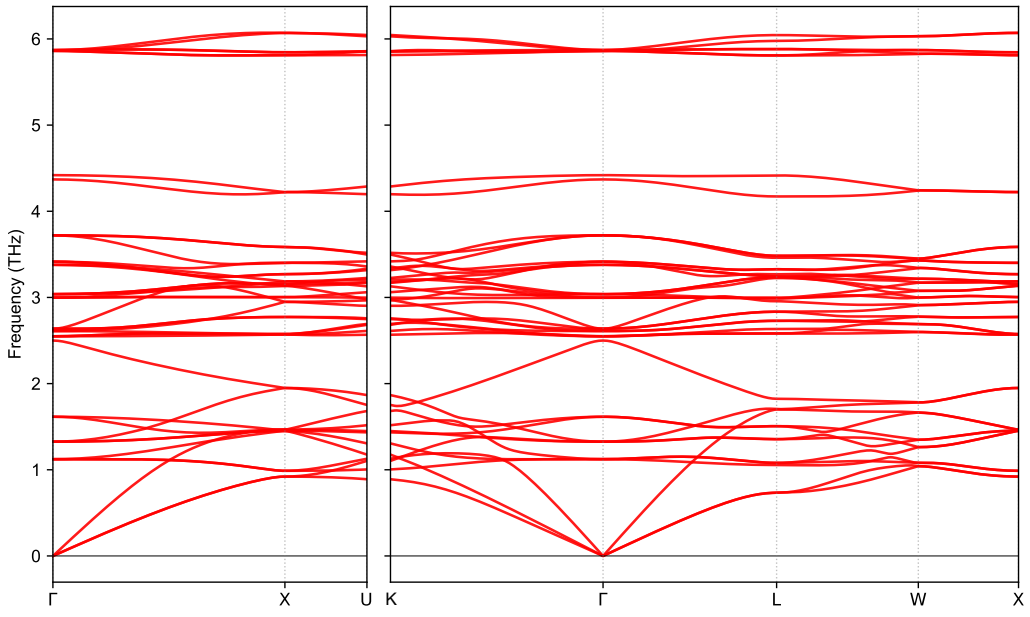

Fig. S23 Phonon band structure of $MgLu_2Te_4$

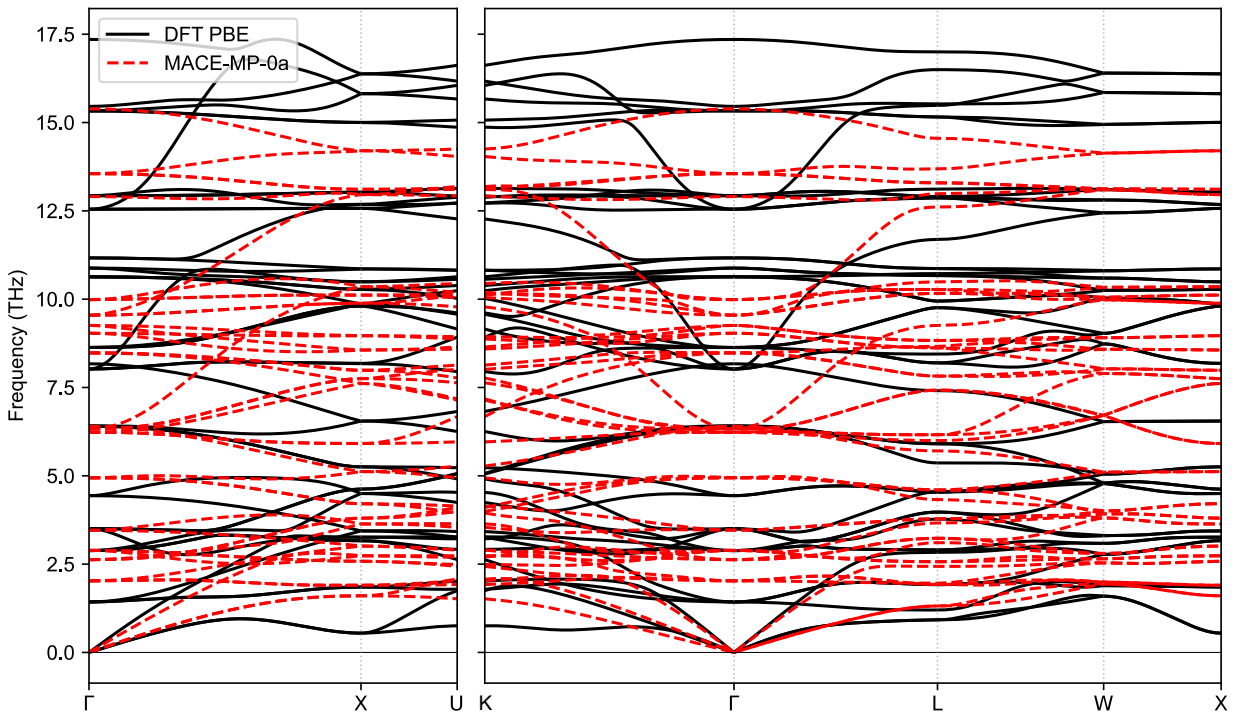

Fig. S24 Phonon band structure of $BaNd_2O_4$

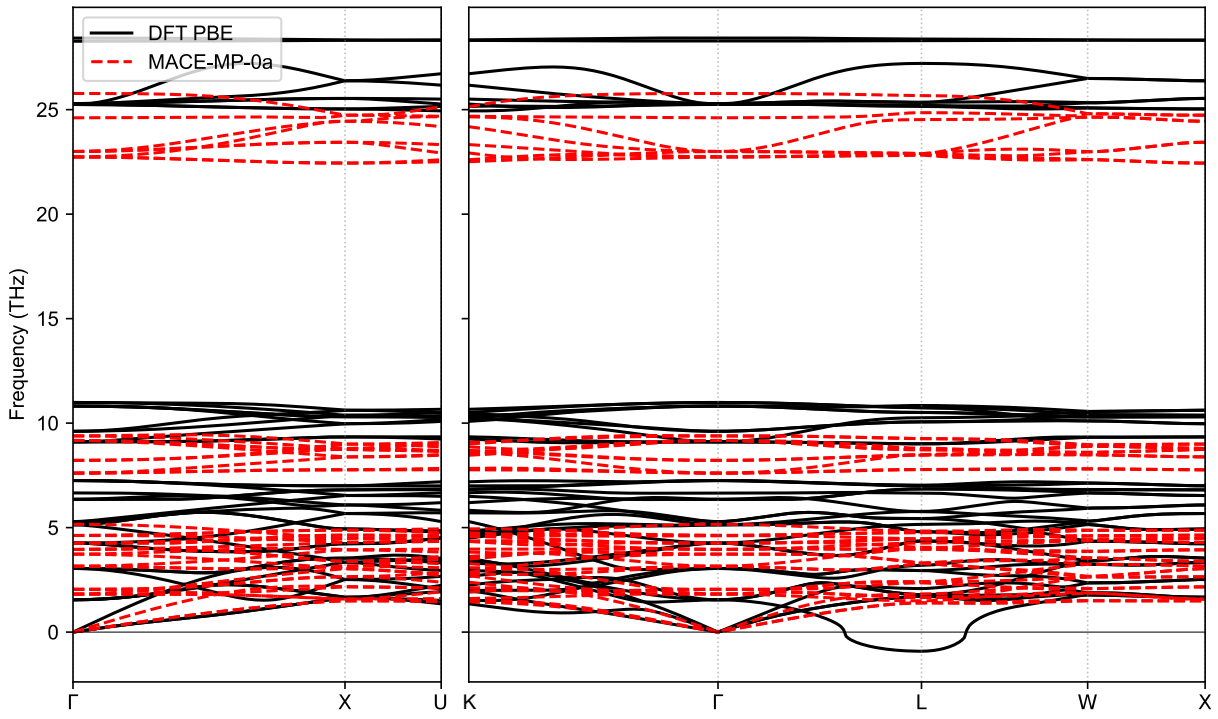

Fig. S25 Phonon band structure of WK_2O_4

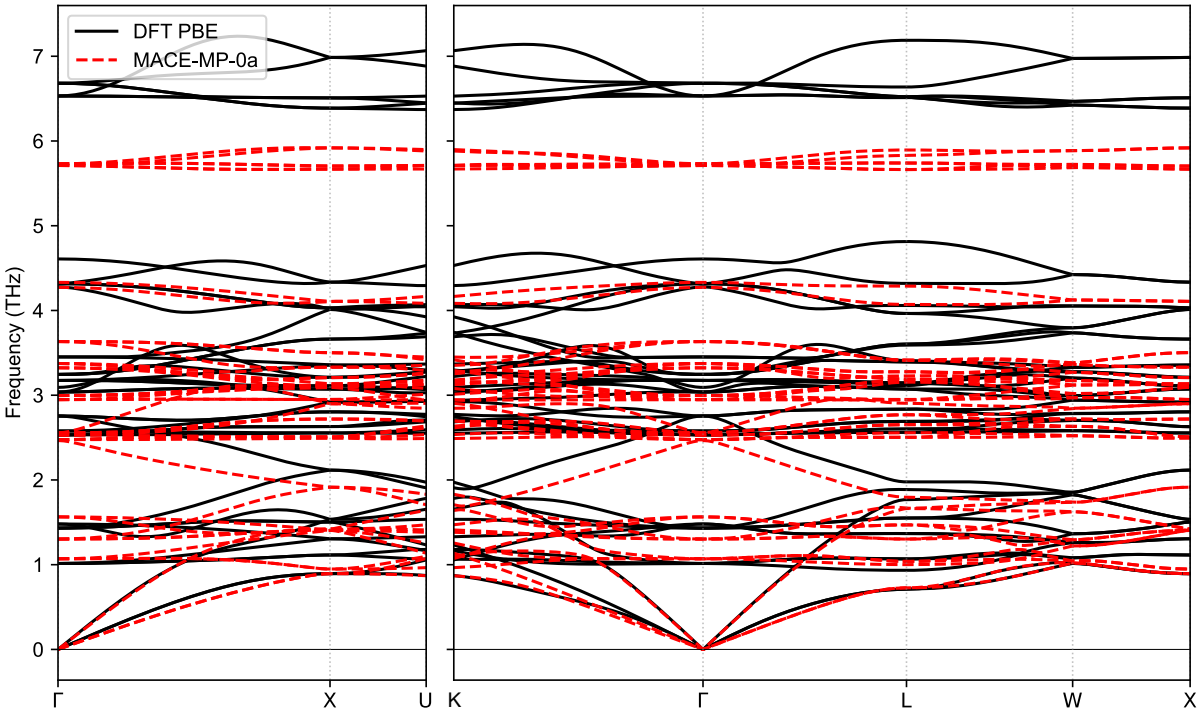

Fig. S26 Phonon band structure of $MgEr_2Te_4$

DFT phonon calculations were carried out using VASP. The analysis was performed using Phonopy[11,12] package. The calculations were carried out using PBE functional with PAW pseudopotentials. The energy cutoff of 520 eV was applied for all systems. The electronic energy convergence criterion was set to 10^{-8} eV. The calculations were performed on a 2×2×2 supercell containing a total of 448 atoms using Gamma-centred 2×2×2 *k*-points alongside Gaussian smearing with a width of 0.05 eV. The results are shown in Fig. S24 to Fig. S26.

Supporting References

1. Hohenberg, P. & Kohn, W. Inhomogeneous Electron Gas. *Phys. Rev.* **136**, B864–B871 (1964).
2. Kohn, W. & Sham, L. J. Self-Consistent Equations Including Exchange and Correlation Effects. *Phys. Rev.* **140**, A1133–A1138 (1965).
3. Perdew, J. P., Burke, K. & Ernzerhof, M. Generalized Gradient Approximation Made Simple. *Phys. Rev. Lett.* **77**, 3865–3868 (1996).
4. Blöchl, P. E. Projector augmented-wave method. *Phys. Rev. B* **50**, 17953–17979 (1994).
5. Kresse, G. & Joubert, D. From ultrasoft pseudopotentials to the projector augmented-wave method. *Phys. Rev. B* **59**, 1758–1775 (1999).
6. Kresse, G. & Furthmüller, J. Efficiency of ab-initio total energy calculations for metals and semiconductors using a plane-wave basis set. *Computational Materials Science* **6**, 15–50 (1996).
7. Kresse, G. & Furthmüller, J. Efficient iterative schemes for *ab initio* total-energy calculations using a plane-wave basis set. *Phys. Rev. B* **54**, 11169–11186 (1996).
8. Batatia, I., Kovacs, D. P., Simm, G. N. C., Ortner, C. & Csanyi, G. MACE: Higher Order Equivariant Message Passing Neural Networks for Fast and Accurate Force Fields. in (2022).
9. Batatia, I. *et al.* A foundation model for atomistic materials chemistry. Preprint at https://doi.org/10.48550/arXiv.2401.00096 (2023).
10. Batatia, I. *et al.* The design space of E(3)-equivariant atom-centred interatomic potentials. *Nat Mach Intell* **7**, 56–67 (2025).
11. Togo, A., Chaput, L., Tadano, T. & Tanaka, I. Implementation strategies in phonopy and phono3py. *J. Phys.: Condens. Matter* **35**, 353001 (2023).

12. Togo, A. First-principles Phonon Calculations with Phonopy and Phono3py. *J. Phys. Soc. Jpn.* **92**, 012001 (2023).